Research Article | Vol. 26, No. 19 | 17 Sep 2018 | OPTICS EXPRESS 25381
Optics EXPRESS

Convex blazed grating of high diffraction efficiency fabricated by swing ion-beam etching method

Chen Shen,[1,2] Xin Tan,[1,*] Qingbin Jiao,[1] Wei Zhang,[1] Na Wu,[1] Heshig Bayan,[1] and Xiangdong Qi[1]

[1]*Changchun Institute of Optics, Fine Mechanics and Physics, Chinese Academy of Sciences, Changchun Jilin 130033, China*
[2]*Univesity of Chinese Academy of Sciences, Beijing 100049, China*
[*]*xintan_grating@163.com*

Abstract: A swing ion-beam etching method to fabricate convex blazed gratings used in shortwave infrared hyperspectral imaging spectrometers is presented. This method solves the consistency problem of blaze angles by swing etching through the meridian direction of the gratings. The mathematical relationship of the curvature, aperture, and diffraction efficiency of convex gratings is studied to demonstrate the limitation of conventional translational lithography and the necessity of swing etching. A geometric model is built to analyze the influence of swinging speed and beam slit width on groove evolution. Convex gratings with a 45.5 gr/mm groove density, 67 mm aperture, 156.88 mm radius of curvature, and 2.2° blaze angle have been fabricated and measured where the peak and average diffraction efficiency in the shortwave infrared band reach 90% and 70%, respectively. Experimental results validate that high-efficiency convex gratings of small blaze angle and high groove consistency can be produced by swing etching, which satisfy the requirements for high spectral resolution and miniaturization of imaging spectrometers.

1. Introduction

The hyperspectral imaging spectrometer [1–6] is a spectral instrument combining spatial imaging technology and spectral acquisition technique which can obtain spatial information and spectral features of the object simultaneously. It plays an important role in many fields such as geological exploration, environmental monitoring, biochemical analysis, clinical medicine and spaceborne remote sensing [7–11]. The Offner imaging spectrometer [12–14] is one of the most widely used hyperspectral imaging spectrometers with the advantages of large field-of-view, compact structure and low distortion of spectral line. A standard Offner imaging spectrometer consists of three concentric spherical optical elements (two concave mirrors and one convex grating).

As the key component of Offner imaging spectrometers, the convex grating requires the properties of large relative aperture, high diffraction efficiency, high precision of groove density and low stray light to meet the requirements for resolution and portability of imaging spectrometers. There are several methods to fabricate convex gratings: mechanical ruling, direct-write electron-beam lithography [15–18], X-ray lithography [19] and holographic ion-beam etching [20]. Ruled gratings on curved substrates will suffer from low consistency of grating pattern and poor surface roughness and include a high cost and difficulty of manufacture, so it is not applied to fabricate curved gratings. The Jet Propulsion Laboratory in the US have successfully fabricated convex blazed gratings using electron-beam direct writing method [21] and X-ray lithography [22] with a relative peak diffraction efficiency of 90% and 88% respectively. These two methods provide excellent results of high diffraction efficiency and controllable groove profile but also have drawbacks such as low throughput, high cost, limited aperture and ghost lines. In consequence, these methods are not widely used. Nevertheless, the technology for making curved gratings by holographic ion-beam

#334634 https://doi.org/10.1364/OE.26.025381
Journal © 2018 Received 17 Jul 2018; revised 26 Aug 2018; accepted 26 Aug 2018; published 14 Sep 2018

etching (H-IBE) is mature. Officine Galileo, NASA, Headwall Photonics, Soochow University [23–26] and other institutions have reported the successful production of convex gratings for imaging spectrometers by holographic ion-beam etching. Compared with the methods above, holographic ion-beam etching has the advantage of no ghost lines, large aperture, low cost and time efficiency. Despite all these strengths, there still exists a problem of the H-IBE method. When we fabricate convex gratings using existing translational ion beam lithography, the blaze angle varies along the grating surface owing to the curvature of the convex substrate and the parallel ion beam. Part of the substrate is not even etched while the designed blaze angle is very small (a few degrees), as show in Fig. 1. This causes low diffraction efficiency and small relative aperture of the convex blazed gratings fabricated by the conventional holographic ion beam etching technology.

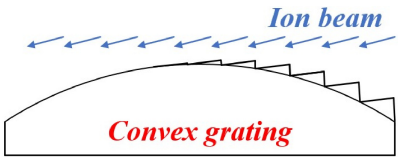

Fig. 1. Sketch of convex grating grooves etched by parallel ion beam.

To solve this problem, the swing ion-beam etching method to fabricate convex blazed gratings of high diffraction efficiency and large relative aperture is presented. In this paper, the relations of the curvature, aperture, blaze angles and diffraction efficiency are studied to illustrate the limitation of conventional translational lithography first. Diffraction efficiencies of convex gratings under different parameters are calculated in Section 2. Then a geometric model of the swing etching process is established to simulate groove evolution under different process parameters in Section 3. The fabrication process of convex gratings with a 45.5gr/mm groove density, 67mm aperture, 156.88mm curvature radius and 2.2° ± 0.2° blaze angle is described in Section 4. These convex gratings would be applied in a meteorological spaceborne hyperspectral imaging spectrometer which requires a wavelength range of 900nm–2500nm and a diffraction efficiency of >65% on average. Finally, the surface topography and diffractive performance of the samples are measured and the experimental results are discussed in Section 5.

2. Limitation of conventional translational lithography

When traditional H-IBE method is used to make a convex grating, the grating pattern on the surface is not consistent, and some parts of the convex substrate are not even etched. We discuss the mathematical relation among the curvature, aperture, ion beam incident angle and diffraction efficiency of the convex grating fabricated by conventional etching method.

2.1 Effect of consistency of blaze angles on diffraction efficiency in meridian direction

A rectangular coordinate system whose origin is the center O of the convex surface is built, as shown in Fig. 2(a). The included angle between the parallel ion beam and the convex surface at the central vertex (tangent plane over the vertex) is θ_0 (grazing angle of ion beam). The curvature radius of the convex surface is R and the aperture of the substrate is L. The equation of the convex surface can be expressed as

$$x^2 + y^2 + z^2 = R^2. \tag{1}$$

P(x, y, z) is an arbitrary point on the grating surface, where α is the included angle of $\overline{PO}$ and the positive direction of y axis, β is the included angle of $\overline{PO}$ and the positive direction of x axis. The direction vector of the parallel ion beam is

$$l = (0, -\cos\theta_0, -\sin\theta_0). \tag{2}$$

Optics EXPRESS

The normal vector of the tangent plane over point P is $\boldsymbol{n}$.

$$\boldsymbol{n} = (-x, -y, -z). \tag{3}$$

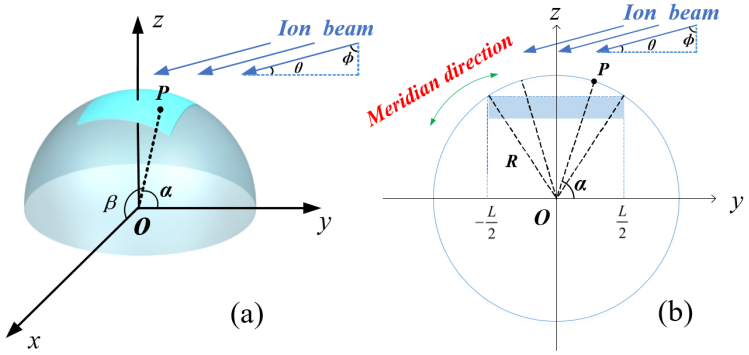

Fig. 2. (a) Schematic diagram of convex surface etched by ion beam. (b) Principal cross-section diagram of the convex grating in the meridian direction.

The included angle of $\boldsymbol{l}$ and $\boldsymbol{n}$ is ϕ. Define $\theta = 90° - \phi$, so we elicit

$$\sin\theta = \cos\phi = \cos\langle \boldsymbol{n}, \boldsymbol{l} \rangle. \tag{4}$$

$$\theta = \arcsin\left(\frac{\boldsymbol{n}\cdot\boldsymbol{l}}{|\boldsymbol{n}||\boldsymbol{l}|}\right) = \arcsin\left(\frac{y\cos\theta_0 + z\sin\theta_0}{R}\right). \tag{5}$$

When $\phi<90°$, $\theta>0$, ϕ is the incident angle of the ion beam on the substrate at point P and θ means the grazing angle of the ion beam; when $\phi>90°$, $\theta<0$, it means the ion beam would no longer graze point P, and this part of substrate surface would remain unetched.

In the case of conventional ion beam etching, we simply consider the effect of curvature in the meridian direction on the consistency of the blaze angles first, that is, calculations are only conducted in the *yoz* plane (the principal section of the grating), as shown in Fig. 2(b). Equations (4) and (5) become

$$\sin\theta = \cos\alpha\cos\theta_0 + \sin\alpha\sin\theta_0 = \sin(\theta_0 + 90^\circ - \alpha). \tag{6}$$

$$\theta = \theta_0 + 90^\circ - \alpha. \tag{7}$$

When the ion beam etches the rectangular photoresist mask with a small grazing angle ($\theta\leq12°$), the blaze angle γ is considered to be approximately equal to θ multiplied by k [27] (the coefficient k is related to the etching rate ratio of the ion beam on substrate materials and photoresist mask; in our experiment $k = 0.63$), namely, $\gamma = k\theta$. From Eq. (7) we can infer the relation between γ and the position on the convex surface is

$$\gamma = \gamma_0 + k(90^\circ - \alpha)\ ,\ \left(90^\circ - \arcsin\left(\frac{L}{2R}\right) \le \alpha \le 90^\circ + \arcsin\left(\frac{L}{2R}\right)\right). \tag{8}$$

where γ_0 is the designed blaze angle, that is, the blaze angle of the groove pattern on the center of the substrate. The magnitude of α is determined by L and R. According to the given parameters such as aperture, radius and grazing angle of the ion beam, the blaze angles at different positions through the meridian direction can be calculated. We can work out the diffraction efficiency curves versus wavelength $\eta(\alpha, \lambda)$ at different points on the grating surface further by using the software PCGrate. Then we fit the results into the overall diffraction efficiency $\eta(\gamma_0, \lambda)$ of the entire convex grating. What calls for special attention is

Optics EXPRESS

that when α is larger than $\theta_0 + 90°$, the value of θ and γ are less than zero, at this time the ion beam will pass over the surface and these areas will remain unetched. Owing to the excellent anisotropy of the ion beam, the unetched areas will keep the original profile of the photoresist mask after etching and still contribute to the diffraction efficiency. They should not be neglected while calculating the diffraction efficiency of the whole grating, so we calculate unetched areas as rectangular photoresist groove profiles. The proportion ψ of the unetched area to the entire surface can be expressed by Eq. (10).

$$\eta(\gamma_0,\lambda)=\left[2\arcsin\left(\frac{L}{2R}\right)\right]^{-1}\int_{90°-\arcsin\left(\frac{L}{2R}\right)}^{90°+\arcsin\left(\frac{L}{2R}\right)}\eta(\alpha,\lambda)\,d\alpha. \tag{9}$$

$$\psi=\begin{cases}\left(\arcsin\left(L/(2R)\right)-\theta_0\right)\Big/\left(2\arcsin\left(L/(2R)\right)\right) & \theta_0<\arcsin\left(L/(2R)\right)\\ 0 & \theta_0>\arcsin\left(L/(2R)\right)\end{cases}. \tag{10}$$

The diffraction efficiency of convex gratings under different parameters are calculated. The grating groove density is 45.5 gr/mm, spectral range of the wavelengths is 900–2500 nm, the diffraction order is −1 level, and the light incident angle is 23.1°. The proportion τ of L and R is taken at 0.05 intervals from 0.05 to 0.5, the grazing angle θ_0 of ion beam at the central vertex is taken at 1.5° intervals from 2° to 8°, that is, $\tau = L/R \in [0.05,0.5]$ and $\theta_0 \in [2°,8°]$. The proportion of unetched area and the range of blaze angles γ on the grating surface with different parameters are given in Table 1. It indicates that there exists unetched areas on the grating surface to every θ_0 when L/R is larger than 0.25. The inconsistency of blaze angles and the size of unetched area are both positively correlated to L/R. θ_0 has little effect on the range of blaze angles, so increasing θ_0 cannot solve the problem of blaze angles' inconsistency.

Table 1. The proportion of unetched area and the range of blaze angles γ under different parameters.

θ_0(*Degree*)		2°	3.5°	5°	6.5°	8°
L/R	0.05	0% (0.36, 2.16)	0% (1.30, 3.11)	0% (2.25, 4.05)	0% (3.19, 5.00)	0% (4.14, 5.94)
	0.10	15.1% (0, 3.07)	0% (0.40, 4.01)	0% (1.34, 4.96)	0% (2.29, 5.90)	0% (3.23, 6.85)
	0.15	26.8% (0, 3.97)	9.3% (0, 4.91)	0% (0.44, 5.86)	0% (1.39, 6.80)	0% (2.33, 7.75)
	0.20	32.6% (0, 4.88)	19.5% (0, 5.82)	6.4% (0, 6.77)	0% (0.48, 7.71)	0% (1.42, 8.66)
	0.25	36.1% (0, 5.78)	25.6% (0, 6.73)	15.2% (0, 7.67)	4.7% (0, 8.62)	0% (0.52, 9.56)
	0.30	38.4% (0, 6.70)	29.7% (0, 7.64)	21.0% (0, 8.59)	12.3% (0, 9.53)	3.6% (0, 10.48)
	0.35	40.1% (0, 7.61)	32.6% (0, 8.55)	25.2% (0, 9.50)	17.8% (0, 10.44)	10.3% (0, 11.39)
	0.40	41.3% (0, 8.53)	34.8% (0, 9.47)	28.3% (0, 10.42)	21.8% (0, 11.36)	15.3% (0, 12.31)
	0.45	42.3% (0, 9.45)	36.5% (0, 10.40)	30.8% (0, 11.34)	25.0% (0, 12.29)	19.2% (0, 13.23)
	0.50	43.1% (0, 10.38)	37.9% (0, 11.33)	32.7% (0, 12.27)	27.6% (0, 13.22)	22.4% (0, 14.16)

Calculation results of diffraction efficiency are shown in Fig. 3. Figure 3(a) shows the ideal diffraction efficiency curve of the convex blazed grating (blaze angle is 2.2172°, at this time the ion beam grazing angle is 3.5°) whose groove profiles are absolutely consistent. The diffraction efficiency curve of the rectangular profile of the photoresist mask without etching is also presented in Fig. 3(a). As seen from Fig. 3(a), the ideal diffraction efficiency curve (colored in black) is much higher than the rectangular mask (colored in red) at each wavelength and its peak value is more than 95%.

Figures 3(b)-3(f) show the diffraction efficiency curves of the convex gratings etched under different curvatures, apertures and grazing angles. Diffraction efficiencies under all parameters are much lower than ideal. The diffraction efficiency of the entire convex grating decreases when L/R increases. This is because when L/R increases, the inconsistency of blaze angles and the size of unetched area become larger as presented in Table 1. Figure 3 also shows the effect of θ_0. The more θ_0 deviates from 3.5°, the lower the diffraction efficiency becomes. Because the variation of the value of blaze angle γ caused by θ_0 will decrease the

Optics EXPRESS

light energy in the designed wavelength band which manifests the left or right shift of the peak of diffraction efficiency curves and the reduction of average diffraction efficiency.

It is concluded that convex gratings with a small blaze angle having good consistency of blaze angles and high diffraction efficiency cannot be fabricated by conventional translational lithography. In our experiment, the grazing angle of the ion beam is 3.4728° and the L/R of the convex substrate is 0.4271. From Fig. 3 and Table 1 we find that convex gratings of such parameters made by conventional method are far from the design needs as the variation range of blaze angles is larger than 0-9.47° and the average diffraction efficiency is less than 20%. Therefore, it is necessary to investigate the swing etching process which can solve the consistency problem.

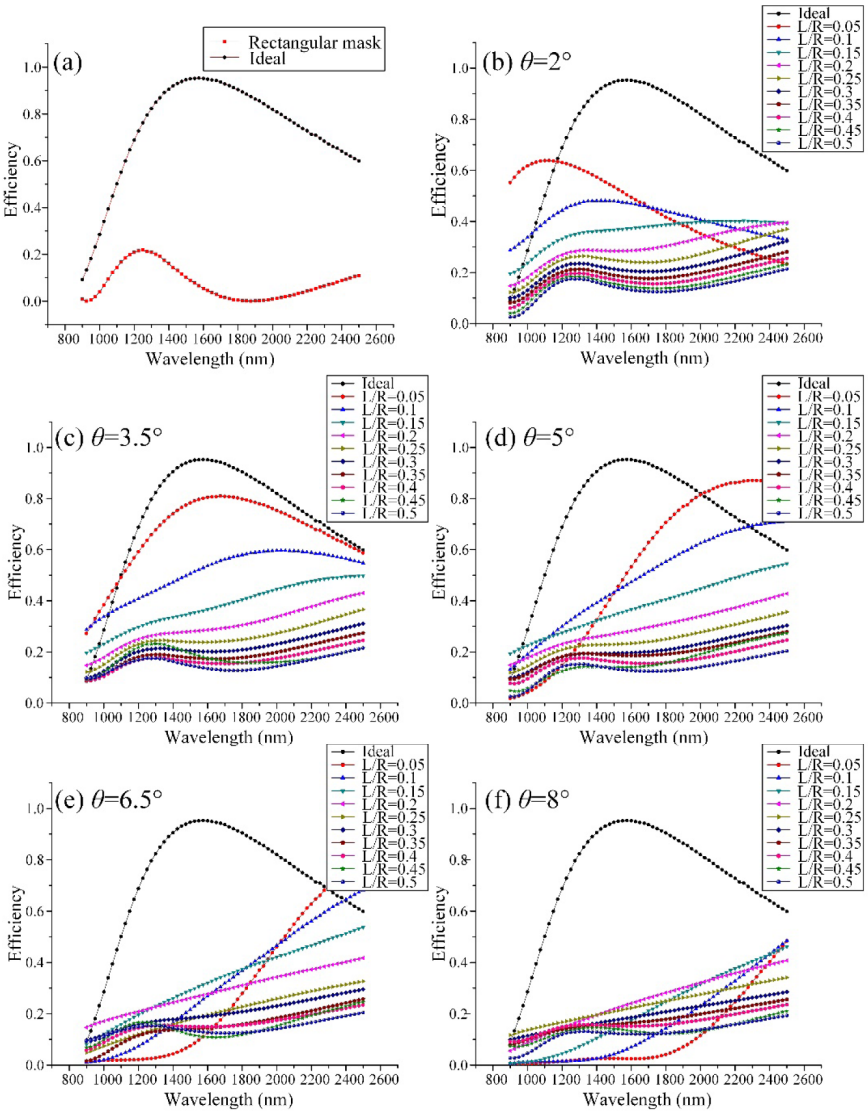

Fig. 3. Diffraction efficiency-wavelength curves. (a) Comparison of diffraction efficiency between ideal grooves and rectangular mask grating; (b)–(f) Comparison of diffraction efficiency between ideal grooves and calculated results of grazing angle θ 2°–8° and τ 0.05–0.5.

Optics EXPRESS

2.2 Effect of consistency of blaze angles on diffraction efficiency in sagittal direction

Swing etching technique sets the curvature center of convex surface as the swinging center O and the curvature radius of the grating as the swinging radius so that the reciprocating swinging motion of the substrate is carried out along the meridian direction around the axis perpendicular to the principal plane which passes through point O, as shown in Fig. 4(a). This method ensures that every point on the convex surface is etched at the same ion beam incident angle in the meridian direction. This makes blaze angles in the meridian direction consistent, but it cannot eliminate the deviations arising from the ion beam incident angles and blaze angles in the sagittal direction. It is impossible to achieve perfectly consistent blaze angles along the entire substrate surface just by swing etching. Therefore, a partition-swing etching method is proposed to solve this problem, as shown in Fig. 4(b). The partition method improves the consistency of the blaze angles by reducing the variation range of ion beam grazing angles in the sagittal direction. Here the effect of the consistency of the blaze angles in the sagittal direction on the diffraction efficiency is investigated.

The ion beam grazing angles are consistent in the meridian direction by swing etching, that is, the variation of grazing angle is irrelevant to y, calculations are only conducted in the xoz plane. Taking $y = 0$, then Eq. (5) becomes

$$\theta = \arcsin\left(\sin\beta\sin\theta_0\right). \tag{11}$$

$$\gamma = k\arcsin\left(\sin\beta\sin\theta_0\right). \tag{12}$$

According to the given parameters of the gratings and etching process, the diffraction efficiency curves $\eta(\beta, \lambda)$ at different points in the sagittal direction are calculated by PCGrate.

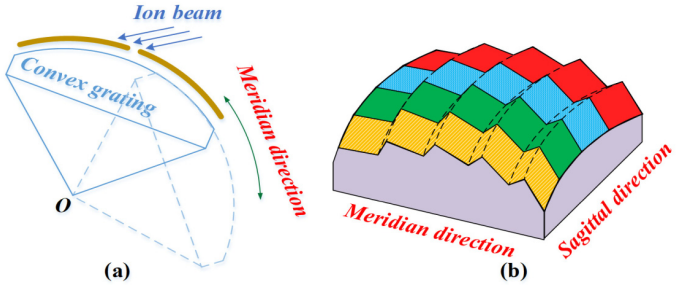

Fig. 4. (a) Sketch of swing ion-beam etching; (b) Partition method in sagittal direction.

Divide the convex surface into n strip-shaped areas along the sagittal direction. The central angle of each strip-shaped area in the sagittal direction is $2\arcsin(L/(2R))/n$ and the grazing angle at the area center is θ_0 as required. In each area we have

$$90^\circ - \frac{1}{n}\arcsin\left(\frac{L}{2R}\right) \le \beta \le 90^\circ + \frac{1}{n}\arcsin\left(\frac{L}{2R}\right). \tag{13}$$

The range of blaze angles is

$$k\arcsin\left(\cos\left(\frac{1}{n}\arcsin\left(\frac{L}{2R}\right)\right)\sin\theta_0\right) \le \gamma \le \gamma_0. \tag{14}$$

Owing to the symmetry of the convex surface, the diffraction efficiency of each area is expressed in Eq. (15). Through the partition method, the groove patterns of the strip areas are the same for they are etched under the same conditions. Therefore, the overall diffraction efficiency of the entire convex grating $\eta(\gamma_0, \lambda)$ is equal to η_n.

Optics EXPRESS

$$\eta(\gamma_0,\lambda)=\eta_n=n\left[\arcsin\left(\frac{L}{2R}\right)\right]^{-1}\int_0^{\frac{1}{n}\arcsin\left(\frac{L}{2R}\right)}\eta(\beta,\lambda)d\alpha. \tag{15}$$

Equations above are utilized to calculate the diffraction efficiencies and blaze angles under the same parameters used in Section 2.1. Table 2 presents the deviation range of blaze angles under different parameters while the number of striped areas is 1(not partitioned). It illustrates that the variation range of blaze angles is positively correlated to θ_0 and L/R in the sagittal direction, and the variation ranges of blaze angles under all parameters are very small as the maximum range is no more than 0.2°. This means that when the ion beam grazing angle varies from 2° to 8°, the blaze angles just change slightly and do not have a distinct effect on diffraction efficiency, as shown in Fig. 5. Calculation results of the diffraction efficiency curves under each parameter are close to those of gratings having completely consistent blaze angles. In our experiment, the range of blaze angles is calculated as 0.049° by swing etching which fully meet the requirement 2.2° ± 0.2°.

Table 2. The deviation range of blaze angles γ under different parameters on grating surface while n = 1.

θ_0(*Degree*)		2°	3.5°	5°	6.5°	8°
L/R	0.05	(1.2666, 1.2670)	(2.2166, 2.2172)	(3.1665, 3.1675)	(4.1165, 4.1178)	(5.0664, 5.0680)
	0.10	(1.2654, 1.2670)	(2.2145, 2.2172)	(3.1635, 3.1675)	(4.1126, 4.1178)	(5.0616, 5.0680)
	0.15	(1.2634, 1.2670)	(2.2110, 2.2172)	(3.1586, 3.1675)	(4.1061, 4.1178)	(5.0536, 5.0680)
	0.20	(1.2606, 1.2670)	(2.2061, 2.2172)	(3.1516, 3.1675)	(4.0970, 4.1178)	(5.0424, 5.0680)
	0.25	(1.2571, 1.2670)	(2.1998, 2.2172)	(3.1426, 3.1675)	(4.0853, 4.1178)	(5.0280, 5.0680)
	0.30	(1.2527, 1.2670)	(2.1921, 2.2172)	(3.1316, 3.1675)	(4.0710, 4.1178)	(5.0103, 5.0680)
	0.35	(1.2474, 1.2670)	(2.1830, 2.2172)	(3.1185, 3.1675)	(4.0539, 4.1178)	(4.9893, 5.0680)
	0.40	(1.2414, 1.2670)	(2.1724, 2.2172)	(3.1033, 3.1675)	(4.0342, 4.1178)	(4.9650, 5.0680)
	0.45	(1.2345, 1.2670)	(2.1603, 2.2172)	(3.0861, 3.1675)	(4.0117, 4.1178)	(4.9372, 5.0680)
	0.50	(1.2268, 1.2670)	(2.1468, 2.2172)	(3.0667, 3.1675)	(3.9865, 4.1178)	(4.9061, 5.0680)

It is concluded that when we fabricate convex gratings by swing etching, the variation range of blaze angles in the sagittal direction is so small that it has little influence on the diffraction efficiency if the grazing angle is small. Therefore, the partition-swing etching method is unnecessary when fabricating convex gratings with a small blaze angle. The requirements for diffraction efficiency could be met simply by swing etching in the meridian direction.

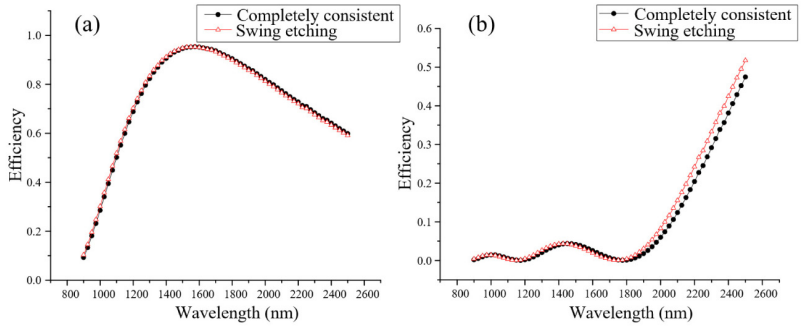

Fig. 5. Comparison of diffraction efficiency between gratings with completely consistent blaze angles and gratings by swing etching. (a) τ = 0.4, θ_0 = 3.5°; (b) τ = 0.5, θ_0 = 8°.

3. Modeling the swing ion-beam etching process

In general, for pattern transfer during the etching process, it is important to find the relationship between etching rate and incident angle of the ion beam, because the incident angle varies along the convex surface under parallel ion beam while other parameters like ion energy, beam density remain constant. In this paper, we obtain the relationships between

Optics EXPRESS

etching rates of different materials and incident angles of the ion beam through experimental measurements combined with the empirical formula given by Ducommun [28]. When the ion beam approaches the normal incidence (ϕ<12°), the etching rate is approximately linear to the incident angle ϕ; when the ion beam grazes the surface (θ<12°), the etching rate is nearly proportional to the grazing angle θ.

The groove evolution under ideal conditions (ion beam incident angles are constant) is analyzed at first. The height and width of the rectangular photoresist mask on the substrate are h and w respectively. The grating period is d and the grazing angle of the ion beam is θ_0. The designed blaze angle is γ and the anti-blaze angle is β. The etching rate of the ridge and the sidewall of the mask are V_h and V_w respectively, and the etching rate of the blazing facet and the anti-blazing facet are V_γ and V_β respectively. To obtain a standard sawtooth groove pattern at the end of the etching process, the mask must be etched out completely just in time, as shown in Fig. 6, so the mask's aspect ratio satisfies Eq. (16). The projection cut-off point E of the ion beam and the blazing facet move along as the height of the mask decreases and they should have the same speed in the horizontal direction [27].

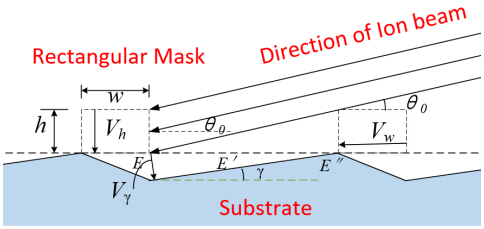

Fig. 6. Groove evolution under ideal condition.

$$h/w = V_h/V_w. \tag{16}$$

$$\tan\theta_0 = h/(d-w). \tag{17}$$

$$V_\gamma/\sin\gamma = V_h/\tan\theta_0. \tag{18}$$

The ion beam grazing angle θ is small enough to apply the small angle approximation in Eq. (19) when making a convex grating with a small blaze angle. k_h and k_w, and k_γ and k_β are the etching rate coefficients of the mask and substrate materials respectively. The following equations could be derived.

$$\sin\theta_0 \approx \theta_0 \approx \tan\theta_0. \tag{19}$$

$$\begin{cases} V_h = k_h\theta_0 \\ V_w = k_w\theta_0 + V_0 \\ V_\gamma = k_\gamma(\theta_0 - \gamma) \\ V_\beta = k_\beta(90^\circ - \theta_0 - \beta) + V_0' \end{cases}. \tag{20}$$

$$\gamma = k_\gamma\theta_0/(k_\gamma + k_h). \tag{21}$$

As shown in Fig. 7, the substrate is swept repeatedly by the ion beam throughout the baffle slit as the 3D-stage swings reciprocally. The effective etching time T_e refers to the time only when the substrate surface was bombarded by the ion beam. The total time of swing etching is T, the etching time in a single swing is t_n, the frequency of swings (semi-periodic number) is n, the swinging speed is ω, and the width of the slit $\overline{AB}$ is D (D is the width of the projection of the ion beam on the substrate passing through the slit). The variation range of

Optics EXPRESS

the grazing angle caused by the slit is $-\min\{\Delta\theta,\theta_0\}$ to $\Delta\theta$. The central angle of the convex substrate is $\theta_{grating}$.

$$T = \theta_{grating} T_e \big/ \left(\Delta\theta + \min\{\Delta\theta,\theta_0\}\right). \tag{22}$$

$$T_e = n \cdot t_n = n \cdot \left(\Delta\theta + \min\{\Delta\theta,\theta_0\}\right) \big/ \omega. \tag{23}$$

$$D = 2R \sin\left(\left(\Delta\theta + \min\{\Delta\theta,\theta_0\}\right)/2\right). \tag{24}$$

$$h = V_h T_e = k_h \theta_0 \cdot n t_n. \tag{25}$$

$$w = V_w T_e = \left(k_w \theta_0 + V_0\right) \cdot n t_n. \tag{26}$$

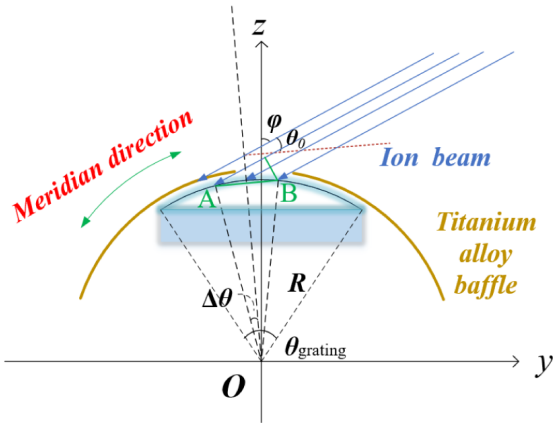

Fig. 7. Parameters of swing etching model.

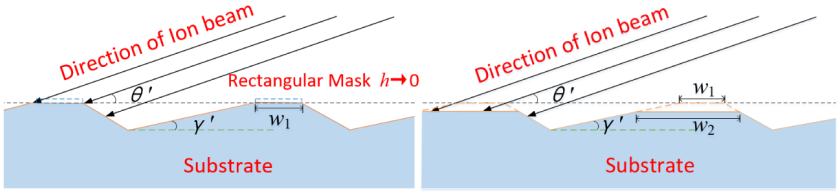

(a) Phase T_1 (b) Phase T_2

Fig. 8. Groove evolution when the slit width is bigger than the critical width.

The mask is just etched out after time T under the ideal condition. Practically, the ion beam grazing angle, etching time and groove evolution are definitely affected by swinging speed ω and slit width D. In each swinging period, the ridge height reduction and mask width shrinkage are h_n and w_n respectively. The total etching amount of the mask during the entire etching process is h' and w'.

(a). When $\Delta\theta \le \theta_0$, that is, $\theta_0 - \Delta\theta \le \theta' \le \theta_0 + \Delta\theta$, the ion beam grazing angle can be written as

$$\theta'(t) = \theta_0 - \Delta\theta + \omega \cdot t \quad , t \in [0, t_n]. \tag{27}$$

$$h_n = \int_0^{t_n} V_h(t)\,dt = \int_0^{t_n} k_h\left(\theta_0 - \Delta\theta + \omega \cdot t\right) dt = k_h \theta_0 \cdot t_n. \tag{28}$$

$$w_n = \int_0^{t_n} V_w(t)\,dt = \int_0^{t_n} \left[k_w\left(\theta_0 - \Delta\theta + \omega \cdot t\right) + V_0\right] dt = \left(k_w \theta_0 + V_0\right) \cdot t_n. \tag{29}$$

Optics EXPRESS

After effective etching time T_e,

$$h' = nh_n = k_h\theta_0 \cdot nt_n = h. \tag{30}$$

$$w' = nw_n = (k_w\theta_0 + V_0) \cdot nt_n = w. \tag{31}$$

In this case, the mean value of the grazing angle is still θ_0, and the blaze angle γ' is unchanged. The evolution of the groove profile is just the same as the ideal situation, so the swinging speed and the slit width do not affect the groove evolution.

(b). When $\Delta\theta > \theta_0$, that is, $0 < \theta \leqslant \theta_0 + \Delta\theta$, a portion of ion beam passes over the surface and cannot bombard the substrate. The mean value of the grazing angles is greater than θ_0, and the blaze angle γ' is increased.

$$\theta'(t) = \omega \cdot t \ , t \in [0, t_n]. \tag{32}$$

$$h_n = \int_0^{t_n} V_h(t)\,dt = \int_0^{t_n} k_h \omega t dt = \left[k_h(\Delta\theta + \theta_0)/2\right] \cdot t_n. \tag{33}$$

$$w_n = \int_0^{t_n} V_w(t)\,dt = \int_0^{t_n} \left[k_w \omega t + V_0\right] dt = (k_w(\Delta\theta + \theta_0)/2 + V_0) \cdot t_n. \tag{34}$$

$$V_h'' = h_n / t_n = k_h\theta_0 + k_h(\Delta\theta - \theta_0)/2 > V_h. \tag{35}$$

$$V_w'' = w_n / t_n = k_w\theta_0 + V_0 + k_w(\Delta\theta - \theta_0)/2 > V_w. \tag{36}$$

$$\gamma' = \frac{k_\gamma}{k_\gamma + k_h} \frac{\Delta\theta + \theta_0}{2}. \tag{37}$$

The average etching rate V_h'' and V_w'' of both the ridge and sidewall of the mask are larger than those of ideal situation in each swinging period, which indicates that the mask will be etched out before the scheduled effective etching time T_e. Furthermore, the etching rate of the ridge increases more than that of the sidewall, that is, the mask will be etched out in the vertical direction in advance so that a flat roof will appear on the top of the groove profile. The over etching of the substrate in the remaining time will increase the width of the flat roof, as shown in Fig. 8.

After time T_1, the mask height is reduced to 0, the width of the flat roof is w_1, and the groove depth is h_1. After time T_e, the final width of the flat roof is w_2 when the etching process is finished. In fact, the grating pattern will not evolve into a standard trapezoidal shape owing to the facet effect. The apex and slot of the groove profile will turn into an arc with a continuously varying slope.

$$h' = \left[k_h(\Delta\theta + \theta_0)/2\right] \cdot T_1 = h. \tag{38}$$

$$w' = (k_w(\Delta\theta + \theta_0)/2 + V_0)T_1. \tag{39}$$

$$T_1 = 2\theta_0 T_e / (\Delta\theta + \theta_0). \tag{40}$$

$$w_1 = w - w' = V_0 T_e(\Delta\theta - \theta_0)/(\Delta\theta + \theta_0). \tag{41}$$

$$w_2 = w_1 + \left(\frac{d - w_1}{h_1}\frac{k_\gamma(\Delta\theta + \theta_0)}{2} - \frac{V_\gamma'}{\sin\gamma'} - \frac{V_\beta'}{\sin\beta'}\right)(T_e - T_1). \tag{42}$$

Optics EXPRESS

We have concluded that, without considering its uniformity, swinging speed has no effect on etching time and groove evolution in the appropriate range (excessive or tiny speed affects the uniformity of the swing and the stability of the workbench). The variation range of grazing angles of the ion beam is positively correlated to slit width. The wider the slit is, the less the total etching time it will cost. When the slit width is less than the critical width $2R\sin\theta_0$, it will not affect the final groove profile; when the slit width is greater than $2R\sin\theta_0$, the blaze angle will increase and a flat roof will appear on the top of groove profile after etching, as well as the size of the blaze angle and the width of the flat roof will be positively correlated to the slit width.

4. Experiment

In Section 2, we concluded that the diffraction efficiency of convex gratings fabricated by conventional method is so low that the swing etching method should be adopted. In Section 3, we investigated the influence of the slit width and swinging speed on groove evolution and several conclusions were reached. In this section, we conducted a series of experiments to verify the consistency of swing etching and the influence of the slit width and swinging speed.

The convex grating specimens were designed for the −1st order in the wavelength range 900–2500nm at the incident angle 23.1° and fabricated according to the optimized designed parameters calculated by the methods in Sections 2 and 3, as shown in Table 3. We spin-coated the positive photoresist on a finely polished and cleaned K9 convex substrate of 67mm × 67mm in area and 1μm in thickness [29,30]. Then we followed the conventional holographic exposure and development steps to form a 45.5 gr/mm grating mask whose ridges were approximately rectangular [31,32]. The real-time monitoring technique [33] and stripe locking technology [34,35] were applied in the exposure and development steps to ensure good groove profile and line precision. Next, we performed ashing with O_2 by inductively coupled plasma etching to remove the residual photoresist in the slot and sidewall burrs of the mask. Meanwhile, the surface roughness and the slot linearity were improved and the duty cycle was reduced by ashing. After that, we transferred the groove pattern from the mask to the convex substrate by swing ion beam etching with the LKQ-200 multifunctional ion beam etcher. The ion beam was generated by the 16cm four-grid RF ion source from Veeco company, whose divergence angle is less than ± 0.1°. The substrate was placed on a 3D hydrocooling stage that could move in arbitrary trajectories by a curve fitting algorithm. We set the ion source and etching parameters according to Table 4. Swinging speed, swing period and slit width were variable while parameters of the ion source were constant to facilitate the study of the etching process. The swing etching process was investigated by changing the combination of these parameters. During the etching process, the substrate on the stage swung reciprocally over a radius of itself. The entire sample was equably scanned at a fixed incident angle by the ion beam coming through the slit, as shown in Fig. 7. After etching, the aluminum coating was deposited on the gratings by magnetron sputtering at the National engineering research center for diffraction gratings manufacturing and application of China. This was to improve the reflectivity and protect the surface. We made a number of grating samples with different swing speeds and slit widths to study the effect of these process parameters on etching results and seek the best process parameters. The morphology of the gratings was tested by an atomic force microscope (AFM). The diffraction efficiency was measured by a homemade multifunctional diffraction efficiency tester.

Table 3. Designed parameters of the mask and convex grating

Aperture	Radius	Period	Mask height	Mask width	Duty cycle	Blaze angle	Roughness
67mm	156.88mm	21.978μm	1000nm	5498.8nm	0.25	2.2° ± 0.2°	<1nm

Optics EXPRESS

Table 4. Swing etching parameters

Ion energy	Beam current	Accelerate voltage	Working gas	Chamber pressure	T_e
500eV	250mA	250V	Ar:CHF_3 = 5:3	~5 × 10^{-2} Pa	165.88min

5. Results and discussion

5.1 Effect of slit width on groove pattern

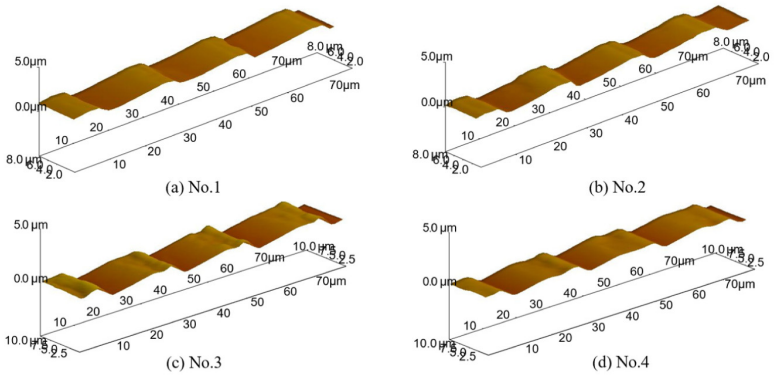

Fig. 9. 3D profile images of samples No.1–4 measured by AFM.

Samples No.1, No.2, No.3, and No.4 were etched with the swinging speed of 0.1277rad/s and slit widths of 23.1mm, 24.8mm, 25.9mm, and 27.3mm, respectively. The slit widths are all larger than the critical width 19mm. Figure 9 shows the 3D surface profiles of the four samples tested by AFM. Figure 10 shows a comparison between the measured cross-section diagrams of the four samples and the simulation results of the swing etching model. As known from the test results, the blaze angles of No.1, No.2, No.3 and No.4 are 2.5979°, 2.7950°, 2.9696° and 3.1301°, respectively. Figures 9 and 10 show that a flat roof appears on the top of the groove profile, and its width becomes larger as the slit width increases. This demonstrates that when the slit is wider than the critical width, the blaze angle is greater than the designed value. Both the size of the blaze angle and the width of the flat roof are positively correlated to the slit width. These results accord with the conclusions elicited in the etching model.

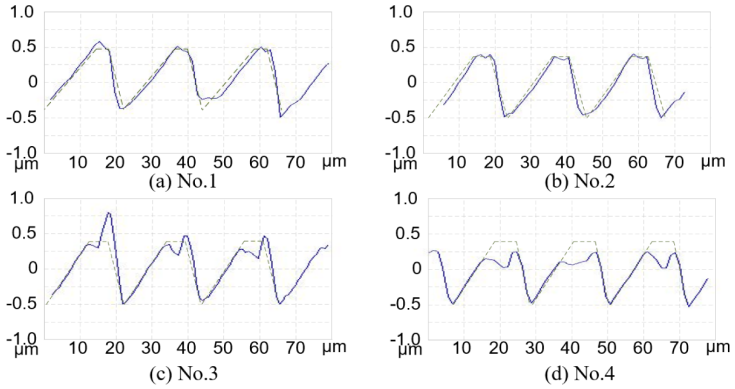

Fig. 10. Measured (solid) and simulated (dashed) cross-section images of samples No.1–4.

Optics EXPRESS

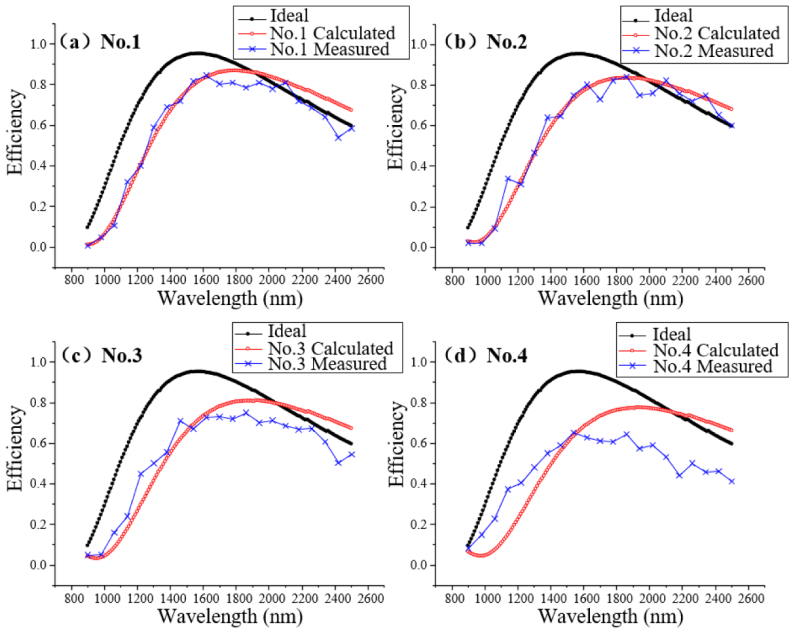

Fig. 11. Measured and calculated results of diffraction efficiency of samples No.1–4.

The groove profiles of the samples are in basic agreement with the simulations of the etching model in Section 3, but there is a certain difference: the measured flat roof width is greater than the calculated result and the flat roof surface is irregular which has ups and downs. The reasons for the discrepancy are as follows: First, the etching model is a simplified geometrical model in which some approximate methods are adopted, so the results are certainly a little different from reality. Second, the incident angle of the ion beam is always changing during the etching process whose influence on the groove formation has not been considered. Third, the total working time cost for the etching process is nearly 10 hours. Therefore, the stability of the ion source would influence the experimental results.

Figure 11 shows the measured and calculated diffraction efficiency curves of samples No.1–4. The calculation results are basically in line with the varying trend of the measured curves. When the slit width is greater than the critical value, the diffraction efficiency will reduce significantly owing to the change of blaze angle. The wider the slit becomes, the lower is the diffraction efficiency. The diffraction efficiency of the grating is severely affected by the increase of blaze angle and groove variation caused by the overwide slit.

5.2 Effect of swinging speed on groove pattern

Figures 12(a) and 12(c) show the groove profile of sample No.5 etched with a swing speed of 0.0064rad/s (linear velocity 1mm/s). Figures 12(b) and 12(d) show the groove profile of sample No.6 etched with a swing speed of 0.0255rad/s (linear velocity 4mm/s). The slit width of both samples is 13.2mm. Figure 13 shows the contrast between the measured diffraction efficiency curves of the two samples and the ideal diffraction efficiency curve. As seen from the diagram, the two samples both exhibit good sawtooth grooves, and their blaze angles are 2.1910° and 2.1928° respectively, which basically meet the designed requirements.

Optics EXPRESS

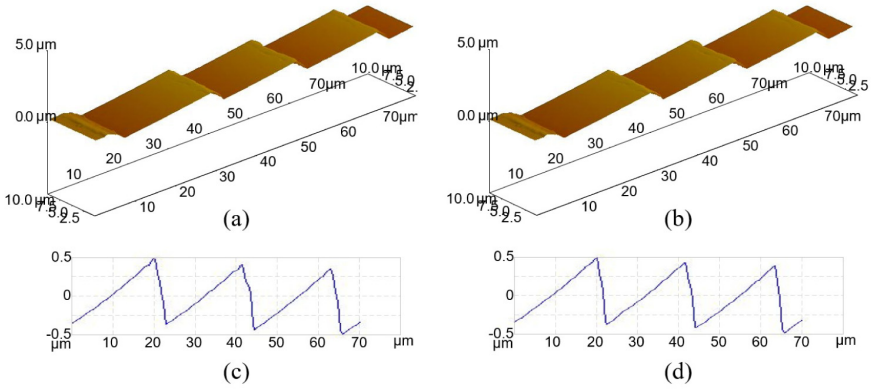

Fig. 12. AFM images: (a) 3D surface profile of sample No.5; (b) 3D surface profile of sample No. 6;(c) cross-section profile of sample No.5; (d) cross-section profile of sample No.6.

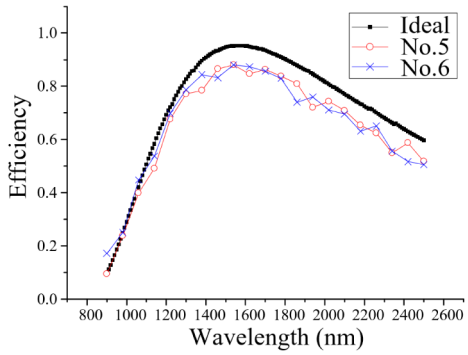

Fig. 13. Comparison between the measured and ideal diffraction efficiency of No.5 and No.6.

The groove patterns of the two samples are basically the same, but the profile of No.6 seems to be a little smoother. This agrees with the conclusion inferred by the model in Section 3, that is, the swinging speed has no effect on the basic shape of grooves, but the influence on the profile details has not been investigated yet. The difference between the two samples may be caused by the effect of swinging speed on the stability of movement of the stage. In this paper, the relation between etching rate and incident angle of the ion beam is approximately treated in the etching model. The effect of the swing uniformity on the incident angle of the ion beam is not considered. Since the track of the stage is controlled by a fitting algorithm, the swing speed is determined by the fitting precision and the motor speed. It is complicated to determine how the swing speed affects the groove evolution in detail. Swinging too slow or too fast will reduce the stability of the stage and the uniformity of motion, which will affect the uniformity of ion beam etching. Therefore, there is an optimal range for the swinging speed that will benefit the etching process.

The diffraction efficiencies of the two samples are similar to the ideal diffraction efficiency, but there is some loss. The peak diffraction efficiency of sample No.5 is 88.03%, and the average diffraction efficiency in the whole wavelength range is 65.07%; the peak diffraction efficiency of sample No.6 is 88.08%, and the average diffraction efficiency is 65.61%. The loss of diffraction efficiency may arise from the following reasons: first, defects on the grating surface reduce the efficiency; second, the inconsistency of blaze angles in the sagittal direction will also have a slight effect on the diffraction efficiency.

Optics EXPRESS

5.3 Blaze angle consistency of swing etching

To verify that the swing etching method can solve the problem of the consistency of blaze angles, groove profiles at different locations on the same convex grating were measured. The location of the different test points is represented by the coordinates (x, y) of their projections

Table 5. Blaze angles at different locations on the substrate surface.

Coordinate (mm)	(a) (−30,-30)	(b) (−30,-0)	(c) (−30,30)	(d) (0,-30)	(e) (0,0)	(f) (0,30)	(g) (30,-30)	(h) (30,0)	(i) (30,30)
Blaze angle	2.1583°	2.1701°	2.1631°	2.2072°	2.2057°	2.1976°	2.1723°	2.1671°	2.1596°

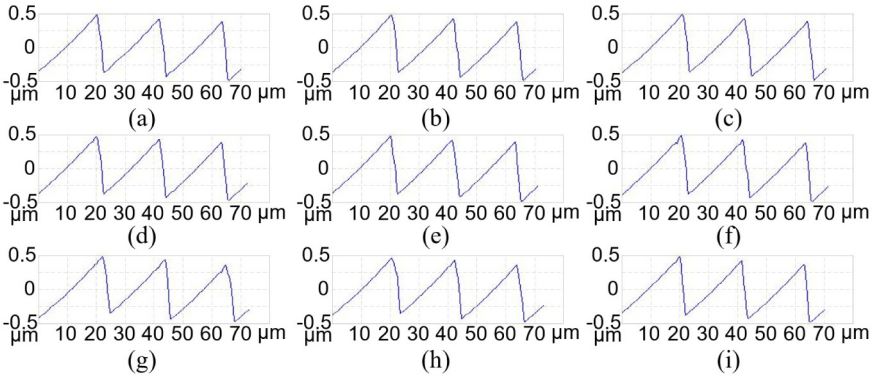

Fig. 14. Cross-section diagrams at different locations on the grating surface by AFM.

on the *xoy* plane. Figure 14 shows the AFM testing results at nine different locations on sample No.7, which was etched with a swinging speed of 0.01rad/s and a slit width of 13.2mm. Table 5 shows the coordinates and the tested blaze angles of different test points. Groove profiles in different locations are basically the same and demonstrate good sawtooth shape. The ranges of blaze angles of three groups of test points (abc, def, and ghi) are 0.0118°, 0.0096° and 0.0127°, respectively, which indicates the high consistency of blaze angles in the meridian direction; the range of blaze angles of three groups of test points (adg, beh, and cfi) are 0.0489°, 0.0386°, 0.0380°, respectively. This shows that the consistency in the sagittal direction is slightly worse. The experiment is basically in line with the calculation results in Section 2. The average blaze angle of the whole grating is 2.1780°, the standard deviation is 0.0187°, the inconsistency is less than 2.2° ± 0.0417°, which satisfy the requirements of the designed tolerance. Compared with conventional methods, the irregularity of the blaze angles of the convex gratings produced by swing etching is much smaller, which proves that the problem of the consistency of the blaze angles on the convex surface could effectively be solved by swing etching method.

5.4 Experimental result of optimized parameters

Considering the effects of the uniformity, stability, etching time and the divergence angle of the ion beam, it is appropriate to choose a moderate swinging speed and a slit width a little less than the critical value. We chose a swinging speed of 0.0127 rad/s and a slit width of 16.5 mm (constrained beam width is 1 mm) to fabricate sample No.8. AFM test results are illustrated in Fig. 15. The sample exhibits a standard sawtooth groove and a blaze angle of 2.2057°. The peak diffraction efficiency of sample No.8 is 90.03% and its average diffraction efficiency of the whole band is 70.25% at the −1st order. The surface roughness of sample No.8 is 0.730 nm (Ra) and 0.893 nm (Rq).

As a contrast, sample No.9 which is fabricated by conventional etching method and sample No.10 which is a rectangular groove grating (laminar) are also measured and exhibited. Figure 16 shows the physical photograph of a convex grating and measured

Optics EXPRESS

diffraction efficiency of samples No.8, No.9 and No.10. The diffraction efficiency curve of sample No.8 is close to the ideal one and much higher than that of samples No.9 and No.10. This strongly validates the necessity and advantage of swing etching and the theoretical calculations in Section 2.

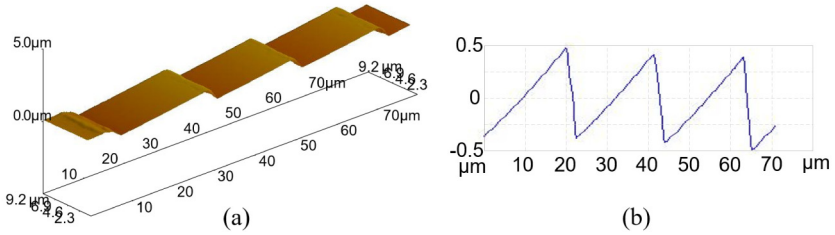

Fig. 15. AFM images of sample No.8: (a) 3D surface profile; (b) cross-section image.

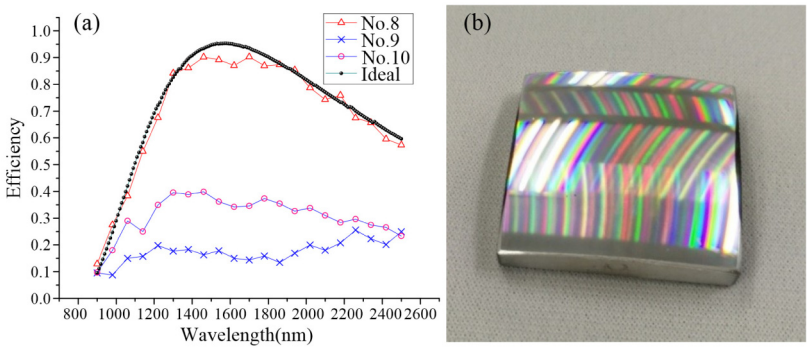

Fig. 16. (a) Comparison between the measured diffraction efficiency of samples No.8, No.9 and No.10 with the ideal efficiency; (b) Photograph of a convex grating.

6. Conclusion

We propose a swing etching method to obtain convex blazed gratings by etching rectangular photoresist masks with the mixture of Ar and CHF_3. First, the influence of the curvature radius and aperture of the grating and the incident angle of the ion beam on the diffraction efficiency of the convex gratings produced by traditional etching method is analyzed. Convex gratings with a small blaze angle made by conventional methods have a low diffraction efficiency. The larger is the relative aperture, the less the diffraction efficiency becomes. This indicates the limitation of conventional translational lithography and the necessity of swing etching in the fabrication of high efficiency and large relative-aperture convex gratings with a small blaze angle. Second, a simple swing etching model is established and the influence of the parameters in the swing etching process on groove evolution is investigated. In good working conditions and appropriate ranges, the swing speed has little effect on the grooves. When the slit is wider than the critical width, the variation of ion beam grazing angles will increase the blaze angle, and a flat roof will appear on the top of the groove after etching. The size of the blaze angle and the width of the flat roof are positively correlated to the slit width. These lead to an appreciable reduction of the diffraction efficiency. This model can be used to calculate the parameters of the swing etching process required by some experiments.

By means of swing etching, we fabricate well-shaped convex gratings with a 45.5 gr/mm groove density, 2.2° ± 0.2° blaze angle, 156.88 mm radius and 67 mm aperture. Convex gratings etched by this method will be of great benefit to imaging spectrometers. The measurement results of AFM and the diffraction efficiency tester show the favorable performance of the samples. An excellent agreement between simulations and measurements is perceived, thereby validating the etching model. Mixing the current working gas with O_2

Optics EXPRESS

can increase the etching rate of the mask thus reducing etching time. However, its flow and effect on the groove evolution need systematic investigation. This requires the optimization of the etching model and process as well as a lot of experimental work. Future works will also include the study of the performance of convex gratings applied in imaging spectrometers.

Funding

National Science and Technology Infrastructure Program of China (2011YQ120023); Major Research Equipment Development Project of Chinese Academy of Sciences (YZ201005); National Youth Foundation of China (61605197).

Acknowledgments

We thank the National engineering research center for diffraction gratings manufacturing and application of China for the use of experimental facilities.

References

1. P. H. Cu-Nguyen, A. Grewe, P. Feßer, A. Seifert, S. Sinzinger, and H. Zappe, "An imaging spectrometer employing tunable hyperchromatic microlenses," Light Sci. Appl. **5**(4), e16058 (2016).
2. X. Prieto-Blanco, C. Montero-Orille, B. Couce, and R. de la Fuente, "Analytical design of an Offner imaging spectrometer," Opt. Express **14**(20), 9156–9168 (2006).
3. J. Reimers, A. Bauer, K. P. Thompson, and J. P. Rolland, "Freeform spectrometer enabling increased compactness," Light Sci. Appl. **6**(7), e17026 (2017).
4. P. Z. Mouroulis and M. M. McKerns, "Pushbroom imaging spectrometer with high spectroscopic data fidelity: experimental demonstration," Opt. Eng. **39**(3), 808–816 (2000).
5. G. Calafiore, A. Koshelev, S. Dhuey, A. Goltsov, P. Sasorov, S. Babin, V. Yankov, S. Cabrini, and C. Peroz, "Holographic planar lightwave circuit for on-chip spectroscopy," Light Sci. Appl. **3**(9), e203 (2014).
6. L. Gao, R. T. Smith, and T. S. Tkaczyk, "Snapshot hyperspectral retinal camera with the Image Mapping Spectrometer (IMS)," Biomed. Opt. Express **3**(1), 48–54 (2012).
7. C. Vannahme, M. Dufva, and A. Kristensen, "High frame rate multi-resonance imaging refractometry with distributed feedback dye laser sensor," Light Sci. Appl. **4**(4), e269 (2015).
8. H. Zhang, T. Wu, L. Zhang, and P. Zhang, "Development of a portable field imaging spectrometer: application for the identification of sun-dried and sulfur-fumigated chinese herbals," Appl. Spectrosc. **70**(5), 879–887 (2016).
9. X. C. Yu, Y. Zhi, S. J. Tang, B. B. Li, Q. Gong, C. W. Qiu, and Y. F. Xiao, "Optically sizing single atmospheric particulates with a 10-nm resolution using a strong evanescent field," Light Sci. Appl. **7**(4), 18003 (2018).
10. S. Mattana, M. Mattarelli, L. Urbanelli, K. Sagini, C. Emiliani, M. D. Serra, D. Fioretto, and S. Caponi, "Non-contact mechanical and chemical analysis of single living cells by microspectroscopic techniques," Light Sci. Appl. **7**(2), 17139 (2018).
11. H. Lin, C. S. Liao, P. Wang, N. Kong, and J. X. Cheng, "Spectroscopic stimulated Raman scattering imaging of highly dynamic specimens through matrix completion," Light Sci. Appl. **7**(5), 17179 (2018).
12. P. Mouroulis, D. W. Wilson, P. D. Maker, and R. E. Muller, "Convex grating types for concentric imaging spectrometers," Appl. Opt. **37**(31), 7200–7208 (1998).
13. R. L. Lucke, "Out-of-plane dispersion in an Offner spectrometer," Opt. Eng. **46**(7), 073004 (2007).
14. Y. Huang, D. Zhang, Z. Ni, and S. Zhuang, "Design of the convex grating imaging spectrometer," in *Conference on Lasers and Electro-Optics/Pacific Rim 2009*, (Optical Society of America, 2009), paper TUP12_18.
15. P. Z. Mouroulis and D. A. Thomas, "Compact low-distortion imaging spectrometer for remote sensing," Proc. SPIE **3438**, 31–37 (1998).
16. M. Okano, T. Yotsuya, H. Kikuta, Y. Hirai, and K. Yamamoto, "Optimization of diffraction grating profiles in fabrication by the electron-beam lithography," in *Diffractive Optics and Micro-Optics*, R. Magnusson, ed. (Optical Society of America, 2002), paper DTuD10.
17. T. Shiono, T. Hamamoto, and K. Takahara, "High-efficiency blazed diffractive optical elements for the violet wavelength fabricated by electron-beam lithography," Appl. Opt. **41**(13), 2390–2393 (2002).
18. W. R. Johnson, D. W. Wilson, and G. Bearman, "All-reflective snapshot hyperspectral imager for ultraviolet and infrared applications," Opt. Lett. **30**(12), 1464–1466 (2005).
19. P. Z. Mouroulis, F. T. Hartley, R. E. Muller, D. W. Wilson, A. Shori, M. Feldman, L. Jiang, and T. R. Christenson, "Grating fabrication through x-ray lithography," Proc. SPIE **5173**, 108–114 (2003).
20. Y. Liu, J. Cui, S. Chen, X. Qi, and Y. Tang, "Design and application of imaging spectrometer with convex grating," Opt. Precision Eng. **20**(1), 52–57 (2012).
21. D. W. Wilson, P. D. Maker, R. E. Muller, P. Z. Mouroulis, and J. Backlund, "Recent advances in blazed grating fabrication by electron-beam lithography," Proc. SPIE **5173**, 115–126 (2003).
22. P. Mouroulis, F. Hartley, D. Wilson, V. White, A. Shori, S. Nguyen, M. Zhang, and M. Feldman, "Blazed grating fabrication through gray-scale Xray lithography," Opt. Express **11**(3), 270–281 (2003).

Optics EXPRESS

23. Headwall Photonics Inc, Hyperspec-VNIR and Hyperspec-NIR, Integrated hyperspectral imaging sensors," http://www.headwallphotonics.com/diffractive-optics-technology.
24. F. M. Reininger, A. Coradini, F. Capaccioni, M. T. Capria, P. Cerroni, M. C. De Sanctis, G. Magni, P. Drossart, M. A. Barucci, D. Bockelee-Morvan, J.-M. Combes, J. Crovisier, T. Encrenaz, J.-M. Reess, A. Semery, D. Tiphene, G. Arnold, U. Carsenty, H. Michaelis, S. Mottola, G. Neukum, G. Peters, U. Schade, F. W. Taylor, S. B. Calcutt, T. Vellacott, P. Venters, R. E. J. Watkins, G. Bellucci, V. Formisano, F. Angrilli, G. Bianchini, B. Saggin, E. Bussoletti, L. Colangeli, V. Mennella, S. Fonti, J.-P. Bibring, Y. Langevin, B. Schmitt, M. Combi, U. Fink, T. B. McCord, W. Ip, R. W. Carlson, and D. E. Jennings, "VIRTIS: Visible Infrared Thermal Imaging Spectrometer for the Rosetta mission," Proc. SPIE **2819**, 66–77 (1996).
25. C. Davis, J. Bowles, R. Leathers, D. Korwan, T. V. Downes, W. Snyder, W. Rhea, W. Chen, J. Fisher, P. Bissett, and R. A. Reisse, "Ocean PHILLS hyperspectral imager: design, characterization, and calibration," Opt. Express **10**(4), 210–221 (2002).
26. Q. Liu, Y. Ji, J. Wu, X. Chen, C. Li, and W. Shen, "Study on convex grating in hyperspectral imaging spectrometers," Proc. SPIE **7494**, 74940N (2009).
27. H. Lin and L. Li, "Fabrication of extreme-ultraviolet blazed gratings by use of direct argon-oxygen ion-beam etching through a rectangular photoresist mask," Appl. Opt. **47**(33), 6212–6218 (2008).
28. J. P. Ducommun, M. Cantagrel, and M. Moulin, "Evolution of well-defined surface contour submitted to ion bombardment: computer simulation and experimental investigation," J. Mater. Sci. **10**(1), 52–62 (1975).
29. S. Yang, X. L. Bayanheshig, X. L. Zhao, S. Xing, Y. X. Jiang, N. Wu, Q. B. Jiao, W. H. Li, and X. Tan, "Establishment and experimental verification of the photoresist model considering interface slip between photoresist and concave spherical substrate," AIP Adv. **5**(7), 077103 (2015).
30. W. Li, X. Bayanheshig, C. Zhang, J. Gao, H. Yu, and Y. Tang, "Application of photoresist melting method to the fabrication of holographic grating," Proc. SPIE **6024**, 60242A (2006).
31. X. Tan, "Fabrication of high-efficiency ultraviolet blazed gratings by use of direct Ar_2-CHF_3 ion-beam etching through a rectangular photoresist mask," Proc. SPIE **8191**, 81910L (2011).
32. B. de A. Mello, I. F. da Costa, C. R. A. Lima, and L. Cescato, "Developed profile of holographically exposed photoresist gratings," Appl. Opt. **34**(4), 597–603 (1995).
33. J. A. Rayas, A. Martínez, R. Rodríguez-Vera, and S. Calixto, "Development in situ for gratings recorded in photoresist," Appl. Opt. **42**(34), 6877–6879 (2003).
34. Y. Song, W. Wang, S. Jiang, Bayanheshig, and N. Zhang, "Weighted iterative algorithm for beam alignment in scanning beam interference lithography," Appl. Opt. **56**(31), 8669–8675 (2017).
35. X. Zhao, W. Bayanheshig, W. Li, J. Yanxiu, Y. Song, X. Li, S. Jiang, and N. Wu, "Moiré alignment algorithm for an aberration-corrected holographic grating exposure system and error analysis," Appl. Opt. **55**(31), 8683–8689 (2016).